Materials Science & Engineering C 112 (2020) 110891

Contents lists available at ScienceDirect

Materials Science & Engineering C

journal homepage: www.elsevier.com/locate/msec

BSA-capped gold nanoclusters as potential theragnostic for skin diseases: Photoactivation, skin penetration, *in vitro*, and *in vivo* toxicity

Cristian R. Lillo[a,d], M. Natalia Calienni[b,c], Belen Rivas Aiello[d], M. Jimena Prieto[b,c], Damián Rodriguez Sartori[d], Jimena Tuninetti[d], Pamela Toledo[c], Silvia del Valle Alonso[b,c], Sergio Moya[e], Mónica C. Gonzalez[d], Jorge Montanari[b,c,*], Galo J.A.A. Soler-Illia[a]

[a] Instituto de Nanosistemas (INS), Universidad Nacional de San Martín-CONICET, Av. 25 de Mayo 1021, San Martín, Buenos Aires, Argentina
[b] Universidad Nacional de Quilmes, Departamento de Ciencia y Tecnología, Laboratorio de Bio-Nanotecnologia, Bernal, Buenos Aires, Argentina
[c] Grupo de Biología Estructural y Biotecnología (GBEyB), IMBICE (CONICET CCT-La Plata), Buenos Aires, Argentina
[d] Instituto de Investigaciones Fisicoquímicas Teóricas y Aplicadas (INIFTA), Facultad de Ciencias Exactas, UNLP-CONICET, CC16 Suc 4 (1900), La Plata, Buenos Aires, Argentina
[e] Centro de Investigación Cooperativa en Biomateriales (CIC BiomaGUNE), 20009 Donostia-San Sebastián, Guipúzcoa, Spain

ARTICLE INFO

Keywords:
Gold nanoclusters
Singlet oxygen
Photoluminescence
Skin penetration
Zebrafish

ABSTRACT

BSA-capped gold nanoclusters are promising theragnostic systems that can be excited to render both fluorescence emission and reactive oxygen species. Although their synthesis and photoluminescence properties are already well described, more accurate information about their use as photosensitizers is required in order to advance towards health applications. In this work, we have obtained BSA-capped gold nanoclusters and characterized their photophysics by different techniques. Singlet oxygen production was detected upon irradiation, which was enough to produce toxicity on two cell lines. Remarkably, an internal energy transfer, probably due to the presence of smaller nanoclusters and the contribution of oxidized residues of BSA in the system, caused fluorescence emission near 640 nm after excitation in the UV range. Additionally, the system was capable of penetrating human skin beyond the stratum corneum, which enhances the potential of these nanoclusters as bifunctional photodynamic therapy effectors and biomarkers with application in a diversity of skin diseases. In the absence of radiation, BSA-capped gold nanoclusters did not cause toxicity *in vitro*, while their toxic effect on an *in vivo* model as zebrafish was determined.

1. Introduction

Gold nanoclusters (GNC) exhibit interesting potential as biocompatible tools for nanomedical applications in both imaging diagnosis and therapies due to their fluorescent properties, stability, and low toxicity [1–3]. These nanostructures present electronic transitions between HOMO-LUMO energetic levels due to their very small size [4,5]. In comparison to traditional CdSe quantum dots, GNC do not contain toxic heavy metals, which makes them more biocompatible, and thus better candidates for several biomedical applications [5–7].

A way to obtain GNC is by reducing gold cations in the presence of bovine serum albumin (BSA) [4], which acts as a template to limit the growth of the clusters, stabilizing and protecting them from further agglomeration [8]. Protein-stabilized GNC present intense and versatile fluorescence in the visible region, which makes them particularly interesting to be used in biochemical studies. A wide variety of proteins have been used to synthesize fluorescent metallic nanoclusters, *e.g.*, bovine serum albumin (BSA), human serum albumin (HSA), lysozyme and trypsin, among others [9–11]. The so obtained metallic nanoclusters are useful to many applications including catalysis, biosensing, photonic techniques, and imaging [12,13]. The synthesis and fundamental characterization of many types of GNC are widely described in the literature [14–16].

The strong near-infrared (NIR) nature of the emission of GNC and the possibility to excite them in the middle range of the visible spectrum due to their large Stokes shift, makes them potentially useful for applications related to skin therapies and diagnosis. In addition to their biological imaging and chemical sensing applications, GNC have demonstrated potential in photodynamic therapy (PDT), which is a minimally invasive therapeutic procedure to destroy tumor tissue

* Corresponding author at: Universidad Nacional de Quilmes, Departamento de Ciencia y Tecnología, Laboratorio de Bio-Nanotecnologia, Bernal, Buenos Aires, Argentina.
E-mail address: jmontanari@unq.edu.ar (J. Montanari).

https://doi.org/10.1016/j.msec.2020.110891
Received 27 December 2019; Received in revised form 9 March 2020; Accepted 20 March 2020
Available online 21 March 2020

selectively. PDT involves a photosensitizing agent or photosensitizer, which after irradiation with a light source generates reactive oxygen species. Photodynamic therapy (PDT) approaches are useful strategies for the treatment of very different skin-related diseases, from skin cancer [17,18] to leishmaniasis [19,20]. The potential of GNC as photosensitizers and singlet oxygen production has been recognized [21–23], but very few works have studied the production of singlet oxygen by BSA-capped GNC [24], while there are no records of skin penetration studies out of a work on simulation [25], which predicts a big increment in permeability when gold nanoparticles range smaller than 2 nm, *i.e.*, the upper size limit of GNC. In need for *in vivo* testing, zebrafish (*Danio rerio*) is a versatile intermediate model, useful for toxicity evaluation of nanomaterials in general [26,27].

In this work, for the first time to our knowledge, the production of reactive oxygen species by BSA-capped GNC has been tested on the viability of two cell lines. This is also the first time that the penetration of these nanoparticles is demonstrated on an *in vitro* model of human skin, assessing their ability to pass through the *stratum corneum* towards deeper skin layers. Intrinsic toxicity of BSA-capped GNC (both *in vitro* and *in vivo*) was also determined.

2. Materials and methods

2.1. Materials

Gold (III) chloride hydrate ($HAuCl_4$·xH2O 99.995%), bovine serum albumin (BSA, > 98%), furfuryl alcohol (FFA, > 98%), fluorescein (dye content 95%), violet cresyl (dye content ~70%), tetrazolium salt [3-(4,5-dimethyl-thiazol-2-il)-2,5-diphenyl tetrazolium] for MTT assay, Neutral Red, were purchased from Sigma-Aldrich and employed without further purification. Ascorbic acid (99.7%), sodium azide (N_3^-), and NaOH (99.99%) from Biopack were used as received. DMEM, RPMI 1640 medium, fetal bovine serum (FBS), glutamine, penicillin, and streptomycin were purchased from Gibco (Waltham, MA, USA).

2.2. BSA-capped GNC synthesis and characterization

2.2.1. Synthesis

BSA-capped GNC were obtained based on the work of Le Guével et al. [10], with some modifications. Briefly, 100 mg of BSA (> 98%) were dissolved in 5 mL (20 mg/mL) of Milli-Q water and stirred until complete dissolution, then 5 mL of aqueous solution of $HAuCl_4$ 10 mM and 50 μL of a solution of ascorbic acid 0.35 mg/mL were added in a bath at 37 °C with vigorous agitation. After 5 min, 5 mL of NaOH 1 M were added, and the mix was left overnight under those conditions. When the reaction was completed, the solution turned to a characteristic brown color. Samples were purified by dialysis against Milli-Q water to eliminate the excess of unreacted reagents and then gold and BSA were determined by Inductively Coupled Plasma Mass Spectrometry (ICP-MS) in iCAP-Q equipment (Thermo Fischer Scientific, Waltham, MA, USA) and by the Bradford determination method, respectively. For gold determination, samples were previously digested overnight with aqua regia and then neutralized prior to ICP-MS measurements.

2.2.2. Size and zeta potential determination by Dynamic Light Scattering

The size of the BSA-capped GNC and BSA was assessed by Dynamic Light Scattering (DLS). Samples were analyzed at 25 ± 0.1 °C with a Malvern Zetasizer Nano (Malvern Instruments; UK) after appropriate dilutions. Each system was analyzed three times. Zeta potential was determined with the same equipment.

2.2.3. Anisotropy

Time-domain anisotropy experiments were performed with a Jobin-Yvon Spex Fluorolog FL3-11 spectrometer (Horiba Scientific, Edison, NJ, USA). Anisotropy profiles obtained for BSA-capped GNC were fitted by a single exponential with $r(t) = r_0 \times \exp(-t / \theta)$, being the rotational correlation times, θ, and anisotropy at time zero, r_0.

2.2.4. Fourier transform infrared (FTIR) spectroscopy analysis

To confirm the presence and integrity of the BSA in the nanoclusters, IR spectra of lyophilized BSA-capped GNC were obtained with a Bruker EQUINOX 25 spectrometer (Bruker, Billerica, MA, USA) using KBr disks as holders. Spectra were taken in the 4000–400 cm^{-1} range with 1 cm^{-1} resolution. Attenuated Total Reflection Infrared (ATR-IR) spectroscopy was performed with a Nicolet 380 FTIR ATR accessory using a ZnSe crystal and an incident beam angle of 45°.

2.2.5. Circular dichroism (CD) spectroscopy

CD spectra were collected at 20 °C on a Jasco 810 spectropolarimeter (Jasco Corporation, Tokyo, Japan). Far-UV CD spectra were scanned from 185 to 340 nm with a 0.1 cm cell and 2 μM protein concentration. For near-UV CD spectra, wavelength range, protein concentration and path length were 240–340 nm, 21 μM, and 1.0 cm, respectively. Scan speed was set to 50 nm/min with 1 s response time, 0.2 nm data pitch and 1 nm bandwidth. Six scans were averaged for each sample, blank subtracted, and smoothed using a fourth-degree Savitzky–Golay polynomial filter with a 10 point sliding window.

2.2.6. X-ray photoelectron spectroscopy

X-ray photoelectron spectroscopy was performed to determine species of gold present in the BSA-capped GNC. Spectra were obtained under ultra-high vacuum with a SPECS SAGE HR 100 spectrometer with a non-monochromatic X-ray source (magnesium Kα line of 1253.6 eV energy and 252 W), placed perpendicular to the analyzer axis and calibrated using the adventitious C 1s peak at BE = 284.4 eV. The selected resolution for the spectra was 15 eV of pass energy and 0.15 eV/step. All measurements were made in an ultra-high vacuum (UHV) chamber at a pressure around $8 \cdot 10^{-8}$ mbar. An electron flood gun was used to neutralize for charging. To obtain better insight into the chemical environment of different atoms, high-resolution XPS spectra were resolved by Gaussian–Lorentzian fitting until minimum χ^2 values were obtained.

2.3. Determination of photophysical properties

2.3.1. UV–Vis spectra

Attenuation spectra were recorded with a double-beam Shimadzu UV-1800 spectrophotometer (Shimadzu, Kyoto, Japan) in a quartz cuvette at a scan rate of 300 nm/min and 1 nm bandpass.

2.3.2. Photoluminescence measurements

The photoluminescence quantum yield (Φ) was estimated with a Jobin-Yvon Spex Fluorolog FL3-11 spectrometer (*vide supra*) equipped with a 450 W Xe lamp, a monochromator (1 nm bandpass gap) and a red-sensitive R928 PM as detector. Emission spectra were collected exciting at 470 nm, performing identical measurements with fluorescein as photoluminescence reference ($\Phi_{fluorescein} = 0.92$), and at 540 nm, using in this case violet cresyl as photoluminescence reference ($\Phi_{violet\ cresyl} = 0.56$) [28]. The temperature was maintained in a range of 25 ± 0.1 °C with an F-3004 Peltier sample cooler controlled by an LFI-3751 temperature controller (wavelength electronics). For all spectra, a correction was made for the wavelength-dependent sensitivity of both the detector and the source. Additionally, the emission spectra were corrected for Raman scattering by using the associated solvent emission spectrum. Time-resolved luminescence measurements were done with a Jobin-Yvon Spex Fluorolog FL3-11 spectrometer (*vide supra*), equipped for time-correlated single-photon counting (TCSPC). Samples were excited with a 461 nm LED (FWHM ~ 1.21 ns, respectively), operating at 1 MHz repetition rate in the absence and presence of oxygen. Data were globally fitted as a sum of exponentials including the instrument response function deconvolution until optimal values of

χ^2, residuals, and standard deviation parameters were attained.

2.4. Reactive oxygen species production

To study the steady-state generation and quenching of singlet oxygen, air-saturated aqueous suspensions of the BSA-capped GNC in a closed vessel were irradiated with a Rayonet lamp emitting at (350 ± 20) nm. Experiments were performed in the presence and absence of two singlet oxygen scavengers: furfuryl alcohol (FFA) and sodium azide (N_3^-). Oxygen concentration was measured throughout the reaction time with an oxygen-sensitive electrode (Orion97-0899).

To assess the superoxide production, measurements were obtained indirectly by an enzymatic colorimetric method employing a commercial kit for cholesterol quantification (Colestat Wiener Lab, Argentina), determining [H_2O_2]. Calibration curves were performed using standard H_2O_2 commercial solutions.

2.5. Cytotoxicity assays

Cytotoxicity was evaluated by two different assays, MTT and Neutral Red (NR), both in darkness and after irradiation. Assays were performed in two human cell lines: HaCaT (IMBICE-CIC-CONICET, Argentina), immortalized keratinocytes, non-tumoral, which are used as model skin cell line, and HeLa cells (ATCC® CCL-2™), an immortalized classic tumor cell line, useful for testing of potential effectors for PDT [18,29]. Cells were maintained at 37 °C with 5% CO_2 in medium supplemented with 10% heat-inactivated FBS, 100 UI/mL penicillin, 100 μg/mL streptomycin, 0.25 μg/mL amphotericin B, and 2 mM glutamine. HaCaT were maintained in RPMI 1640 and HeLa in DMEM.

For the non-irradiated experiments, cells were seeded at a density of 1×10^4 cells/well in 96-well microplates, and grown for 24 h until 70–80% confluence. Cells were then incubated with 100 μL of BSA-capped GNC for 24 h. Controls in the absence of nanoclusters were included. After incubation, wells were washed with phosphate-buffered saline (PBS), and then, for MTT assay, 0.125 mg/mL of tetrazolium salt in fresh medium were added and, after 90 min at 37 °C, removed. Formazan crystals were dissolved in DMSO, and absorbance was measured at 570 nm with background subtraction at 655 nm in a BIO-RAD 680 microplate reader (CA, USA). For NR assay, after incubation and washing of cell monolayers, 200 μL per well of NR solution (50 μg/mL) were added and left at 37 °C for 2 h. Cells were washed with PBS, and NR was dissolved in 200 μL of acetic acid 1% in ethanol 50%. Absorbance was measured at 570 nm with background subtraction at 690 nm.

To assess the potential of BSA-capped GNC as PDT effectors, the setup was similar to for the experiment in darkness. Controls in the absence of nanoclusters were included. After 2.7×10^3 cells/well were grown for 24 h, samples were added in fresh medium at different concentrations. On the following day, the medium was replaced to eliminate all the BSA-capped GNC that were outside the cells, and then monolayers were irradiated with a UV lamp (400 nm) for 1 h (HeLa) or 30 min (HaCaT), in media without phenol red. Irradiation times were previously determined to be innocuous for each cell line, respectively. After 24 h of irradiation, MTT and RN assays were performed as stated before.

The percentage of cell viability was calculated according to the following equation, where Abs T is the absorbance of treated cells and Abs C is the absorbance of control (untreated) cells:

$$\text{Cell viability (\%)} = \text{Abs T}/\text{Abs C} \times 100$$

2.5.1. Cellular uptake

Cell uptake of the BSA-capped GNC upon incubation on HaCaT cells was assessed by confocal laser scanning microscopy (CLSM; FluoView FV300, Olympus, Tokyo, Japan). Cells were grown 24 h on coverslips in 6-well plates. Following, BSA-capped GNC were incubated during 3 h at 37 °C and then the suspension was removed, cells were washed, and coverslips were excited with a 350 nm laser, and emission was taken with a filter of 647 nm. The images were processed with ImageJ software (US NIH, Bethesda, Maryland, USA).

2.6. Skin penetration assays

2.6.1. Preparation & sample incubation

To assess the penetration of the BSA-capped GNC in the skin, assays were performed *in vitro* with the Saarbrücken Penetration Model (SPM) [30]. Skin explants from an adult woman in healthy conditions, obtained after aesthetic surgery of abdominal reduction, were punched out in the form of disks of 24 mm in diameter, after removal of the hypodermis, and then placed into the SPM device, on a filter paper soaked in Tris buffer. Aliquots of BSA-capped GNC suspensions were applied under non-occlusive conditions and incubated for 1 h at 35 °C [17,31]. All skin penetration protocols were approved by the Ethical Committee of the National University of Quilmes (UNQ) by Resolution CE-UNQ#01-2019, in accordance with the Code of Ethics of the World Medical Association.

2.6.2. Tape stripping and skin cryosectioning

After incubation of five skin specimens of BSA-capped GNC, tape stripping was performed. Briefly, the skin surface was wiped and put on an expanded polystyrene block, stretched by metal pins. A total of 20 strips of adhesive tape (Doble A R, Abrasivos Argentinos SAIC, Buenos Aires, Argentina) were successively placed over the skin disk, charged with a uniform weight (2 kg) during 10 s, and removed to collect the adhered skin layer from the *stratum corneum* (SC) [32]. The remaining skin after the 20 strips, corresponding to viable epidermis and dermis (VED) was cut and homogenized. Tapes were grouped as 1–4 (upper SC), 5–10 (middle SC), and 11–20 (lower SC) [33]. The obtained samples were extracted with ethanol:water (1:1 v/v), and then stirred at 190 rpm (1 h, 37 °C) and the presence of BSA-capped GNC was determined by fluorescence spectroscopy (λ_{ex} 350 nm, λ_{em} 650 nm). For other skin disks, after incubation, samples were frozen, embedded in optimal cutting temperature compound (OCT, from Sigma-Aldrich), and sliced at −20 °C in transversal sections of 20 μm thickness with a Leica CM1850 cryostat (Leica Microsystems, Nussloch, Germany). Specimens were observed by CSLM with the same setup as in Section 2.5.1.

2.7. Toxicity in zebrafish

The toxicological effects *in vivo* of BSA-capped GNC in darkness were determined on zebrafish (*D. rerio*) as recently reported by Calienni et al. [31,34]. In this case, larvae were placed on 96-well plate at 1 day post fecundation (dpf), three individuals per well, and maintained at 28 ± 1 °C with a cycle of 14/10 h of light/dark in E3 medium (NaCl 0.29 g/l, KCl 0.012 g/l, $CaCl_2$ 0.036 g/l and $MgSO_4$ 0.039 g/l and 50 ppb methylene blue in deionized water). At 5 dpf BSA-capped GNC were added. The spontaneous movement was measured during 15 min, at 1, 24, and 48 h post-incubation (hpi) with a W Microtracker device (Designplus SRL, Buenos Aires, Argentina) at room temperature. Results were relativized to the untreated control and reported as the percent of swimming activity. Data were analyzed by one-way analysis of variance and multiple comparisons test of Dunnett, for all studies. Each sample was compared with the control. GraphPad Prism was used to conduct all statistical analyses. Only values with $p < 0.05$ were accepted as significant.

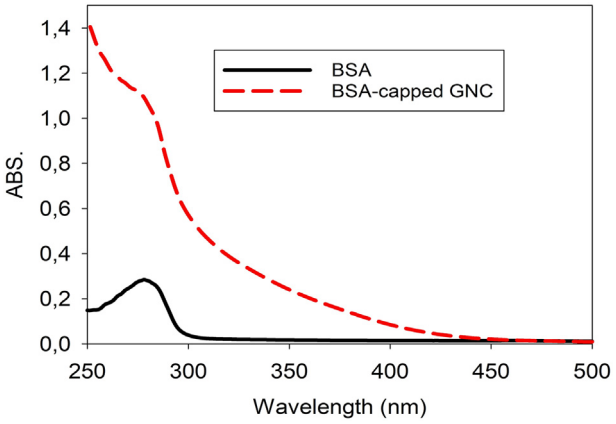

Fig. 1. UV–Vis spectra of BSA (black line) and BSA-capped GNC (red dotted line) adjusted to a final concentration of 0.5 mg/mL of BSA protein in PBS buffer 10 mM pH = 7.4. (For interpretation of the references to colour in this figure legend, the reader is referred to the web version of this article.)

3. Results and discussion

3.1. Characterization of BSA-capped GNC

The used synthesis is expected to render mostly nanoclusters of 25 Au atoms [35]. While larger nanoparticles are not expected to be formed, the presence of a minority of smaller Au clusters has also been reported [10]. UV–Vis and fluorescence spectra are used here to corroborate the nature of the particles that have been obtained in the synthetic procedure.

3.1.1. Absorbance spectra

Fig. 1 shows a UV–Vis attenuation spectra of BSA-capped GNC and BSA aqueous suspensions. The absorption spectrum of the BSA-capped GNC shows strong absorption in the UV that decays exponentially towards the visible, without the presence of the typical plasmon resonance absorption displayed by gold particles of larger sizes, which hints that the structures formed have sizes smaller than 2 nm. Additionally, a small shoulder can be seen at 287 nm, which corresponds to the typical absorption spectrum of the tryptophan residues in BSA protein.

3.1.2. Photoluminescence properties

The photoluminescent properties of BSA-capped GNC are shown in the excitation-emission matrix (EEM) of Fig. 2A and B, obtained for different batches of the same synthesis procedure, in the absence and presence of molecular oxygen, respectively. In these figures, Box A shows the zone of excitation and emission of the Au_{25} nanoclusters and Box C shows the fluorescent properties of smaller clusters, and probably also the contribution of some oxidized residues of BSA [36–38], while box B could represent the EEM of an efficient energy transfer between excited small Au_{8-5} and probably a minor contribution from oxidized amino acids [36] (energy donors) and Au_{25} (acceptor) clusters, as will be discussed further. This phenomenon is easily observed in the excitation and emission spectra shown in Fig. 3. In this figure, graph (B) shows the emission spectra of BSA-capped GNC when they are excited with UV (350 nm) and visible (490 nm) light. The higher peak around 640 nm corresponds to the emission of the Au_{25} clusters while that at around 440 nm is assigned in the literature to the emission of smaller clusters of Au_n ($8 > n > 5$) [10]. It is interesting to note that, UV excitation of Au_{8-5} clusters leads to the emission of Au_{25} nanoclusters, probably due to an energy transfer mechanism, in line with the overlap observed between the excitation spectrum of Au_{25} nanoclusters and the emission peak of the smaller ones. Therefore, the luminescence observed in Fig. 2 Box B may be assigned to Au_{25} emission through an indirect excitation involving an energy transfer mechanism from excited Au_{8-5} nanoclusters. As a consequence Au_{25} excitation spectrum extends well to the UV. Interestingly, in the presence of molecular oxygen, the energy transfer mechanism is preferentially observed, thus indicating that Au_{8-5} clusters are not easily quenched by O_2 probably as a consequence of their short excited state lifetime which prevents an encounter with O_2 limited by diffusion and/or because of their tiny size BSA is able to form a thick surrounding layer preventing a fast diffusion of O_2.

The photoluminescence quantum yield (Φ) of BSA-capped GNC was determined at 470 nm using fluorescein as a reference ($\Phi_{fluorescein} = 0.92$) and at 540 nm using violet cresyl ($\Phi_{violet\ cresyl} = 0.54$), obtaining values of 6% and 2% respectively.

3.1.3. Time decay

The photoluminescence (PL) decay time was obtained from biexponential decay fittings of the PL traces detected at 640 nm upon 341 nm excitation in the absence and presence of oxygen (Fig. 4). The curves could be well fitted to a biexponential function with decay times $\tau_1 = 3.7 \pm 0.2$ ns and $\tau_2 = 428 \pm 6$ ns showing 3% and 97% contribution to the overall fluorescence, respectively, in the absence of oxygen. The decay time τ_2 is in the expected order for Au_{25} nanoclusters [10]. In the presence of oxygen, decay times were $\tau_1 = 3.6 \pm 0.1$ ns and $\tau_2 = 388 \pm 6$ ns. These results nicely prove that incorporated O_2 may efficiently quench the BSA-capped Au_{25} GNC PL due to a dynamic process, as the time decay for GNC is faster when oxygen is present [39]. On the other hand, the emitter contributing to τ_1 could correspond to a population of BSA-capped Au_{25} nanoclusters of different morphology which cannot be reached by molecular oxygen.

3.1.4. Anisotropy

Time-domain anisotropy experiments were performed exciting with light of 341 (Fig. 5A) and 461 nm (Fig. 5B) and detecting the emission at 640 nm. Both anisotropy profiles could be well fitted to a two exponential function with $r(t) = r_{01} \times \exp(-t/\theta_1) + r_{02} \times \exp(-t/\theta_2)$ being θ_i the rotational correlation times and r_{0i} the limiting anisotropies at time zero. In all cases, a fast component θ_1 of 1.3–2.0 ns and a slower one θ_2 of 12–22 ns are observed. Considering that for each Au nanocluster emitter, the anisotropy decays as a single-exponential in agreement with the clusters spherical shape, the observation of a double exponential is compatible with emission mainly originated from different excitation processes. In fact, the occurrence of FRET leads to an anisotropy decay component faster than the slow rotational component of the free fluorophore. Fast anisotropy depolarization of *ca.* 0.5 to 1.5 ns, depending on the separation distance of the donor and the acceptor are reported in the literature due to FRET between fluorophore dimmers [40]. Due to the complexity of the system, we did not analyze further the fast anisotropy depolarization.

Moreover, considering that anisotropy depolarization by fluorophore rotation requires that depolarization occurs during the average time that the fluorophore remains in the excited state ($t \sim 5\tau$), then, only the polarized emission of long-lived Au_{25} emitters is observed at long depolarization times. Taking θ_2 of 12–22 ns, the hydrodynamic diameter of the emitting fluorophore (D) may be obtained by the Stokes–Einstein–Debye relation [31] considering the shear viscosity of water at 300 K ($\eta = 1.00$ mPa s). Values of D within 7.9–9.6 nm are in coincidence within the experimental error, with DLS data.

The FT-IR spectra of lyophilized BSA-capped GNC present the characteristic vibration peaks of the BSA protein (Fig. 6A). The typical bands of protein amide I (1600–1700 cm^{-1}), amide II (~1550 cm^{-1}), and amide III (~1350 cm^{-1}) corresponding to CO stretch and C—N stretch coupled with N—H bending mode respectively. The broad absorption centered at 3280 cm^{-1} corresponds to primary amines and hydroxyl groups, and the peak at 2960 cm^{-1} corresponds to C—H vibration [10]. No substantial changes in the BSA conformation were detected by this technique, although CD revealed the structural

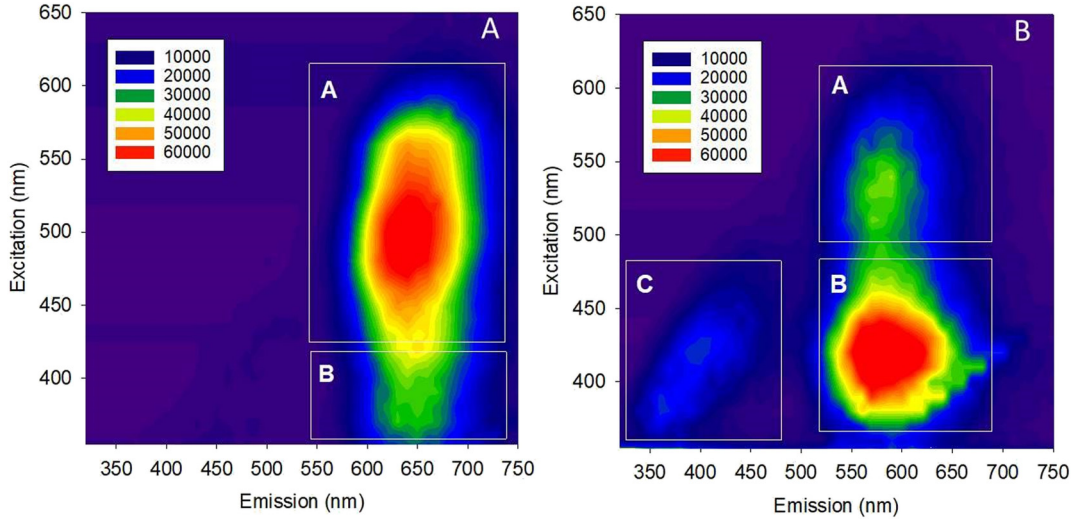

Fig. 2. Excitation-emission matrix of aqueous suspension of BSA-capped GNC under argon and air saturation, figures (A) and (B), respectively. Box A shows the zone of excitation and emission of the Au_{25} nanoclusters; box B represents the energy transfer between the spectra of smaller and Au25 clusters, while box C shows the fluorescent properties of the smaller nanoclusters.

alteration of the protein. Fig. 6B shows the comparative CD spectra in the far-UV between the native BSA and the BSA-capped GNC. The spectra were adjusted to the same amount of protein — determined by the Bradford assay. In the spectrum of BSA present in GNC, the peak near 210 nm of the native BSA appears slightly shifted to lower wavelengths, while the 220 nm peak is lost. Both differences report the loss of the secondary structure of the protein. Similar changes were observed in the CD near-UV spectra (data not shown) corroborating the loss of the native structure of BSA. This phenomenon was reported before by other works [41,42] and it could be due to the highly basic conditions of the synthesis process (pH = 10) that induces ionization of functional groups in some amino acid residues, with the consequent restructuring of the protein surrounding the GNC.

Fig. 7 shows the high-resolution XPS spectrum of the Au 4f core level of the sample satisfying the characteristic 3.7 eV separation of the spin orbit components. The peaks show the 88% contribution of a band with Au 4f7/2 BE of 83.8 eV attributed to Au^0 and a second less significant contribution of *ca.* 12% at 84.5 eV attributed to Au^+. The small content of Au^+ is consistent with that reported by other authors [35]. The C1s signal was used as calibration (284.6 eV).

The hydrodynamic diameter and the Z-potential of BSA-capped GNC and BSA protein were determined by means of DLS measurements. The measurements were made in phosphate buffer at 298 K after sonication of the previously dialyzed samples, a value of D_{DLS} = 8.9 ± 2.2 nm, Zpot = −55 ± 3 mV and D_{DLS} = 7.2 ± 2.1 nm, Zpot = −48 ± 5 mV were obtained respectively, coinciding with reported values by other authors [10,24]. The difference between the hydrodynamic diameter values obtained by DLS for BSA-capped GNC and BSA under the same conditions allows estimating the approximate size of the Au_{25} GNC, namely 1.7 nm, as reported by other works [24,43]. On the other hand, anisotropy analysis also gives information about the size, as the time of Brownian rotation of a fluorophore, θ, gives information on the hydrodynamic diameter (D) by the Stokes–Einstein–Debye relation [44]. Considering the shear viscosity of water at 300 K (η = 1.00 mPa s), D_{ANS} = 7.2 ± 1 nm was obtained for BSA-capped GNC in coincidence, within the experimental error, with DLS data.

A sample of the BSA capped GNC was digested with aqua regia and then neutralized with NaOH to determine the total of gold content by ICP-MS. The value obtained by ICP-MS was converted to mmol of Au_{25}, assuming that this is the only species present, although it is known that there is a small proportion of Au_n ($8 > n > 5$) in the sample. The

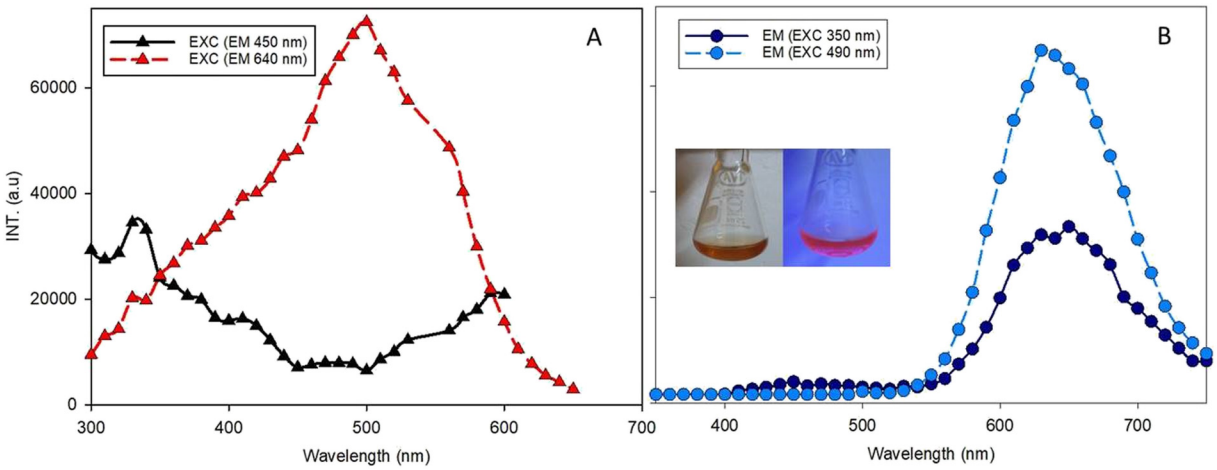

Fig. 3. Fluorescence spectra of BSA-capped GNC. Graph (A) excitation spectrum corresponding to the small emission in the UV (450 nm) and in the visible (640 nm). Graph (B) shows the emission spectra when the system is excited with UV light (350 nm) and with visible light (490 nm). Inset: BSA-capped GNC aqueous suspension irradiated with white light (left) and UV light (right).

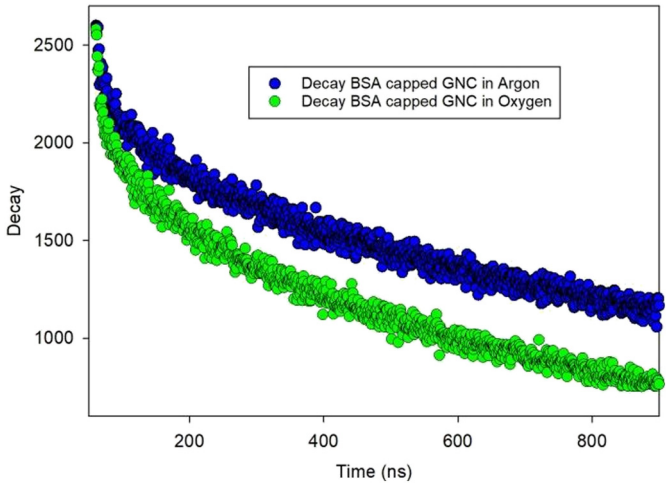

Fig. 4. Time decay BSA-capped GNC in presence (green circles) and absence (blue circles) of oxygen. The PL traces detected at 640 nm upon 341 nm excitation. (For interpretation of the references to colour in this figure legend, the reader is referred to the web version of this article.)

determined value was 0.0013 mmol of GNC per mL (6.6 mg/mL). On the other hand, an aliquot of the same stock of BSA-capped GNC, BSA was determined by the Bradford method obtaining a value of 0.0015 mmol of BSA protein per mL (9.9 mg/mL). These determinations show that approximately one protein molecule exists for each Au_{25} cluster.

3.2. ROS generation

The ability of BSA-capped GNC to produce singlet oxygen (reaction (1) in Fig. 8) was studied through the indirect method of molecular oxygen consumption. To this end, aqueous suspensions of BSA-capped GNC were irradiated in a Rayonet photoreactor equipped with eight 350 nm lamps in the absence and presence of specific $^1O_2$ scavengers, such as furfuryl alcohol (FFA) and sodium azide (N_3^-) [44,45]. The results are shown in Fig. 8, in which it can be observed that the addition of 10^{-3} M FFA to the particle suspension resulted in O_2 depletion (reaction 6 in Fig. 8). Since the FFA is a well-known chemical scavenger of $^1O_2$, this result demonstrates the ability of BSA-capped GNC to produce $^1O_2$ upon 350-nm irradiation. To test this assumption, a physical quencher of $^1O_2$, *i.e.*, N_3^- was added in excess, which was expected to diminish the rate of O_2 depletion due to the competition of N_3^- with FFA for $^1O_2$, as observed experimentally (reaction (4) in Fig. 8). In the absence of chemical $^1O_2$ quenchers, no molecular oxygen consumption was expected due to efficient relaxation of $^1O_2$ to $^3O_2$ (reaction (2) and (3) in Fig. 8).

Formation of superoxide radical anion, O_2^-, upon 350 nm irradiation of aqueous suspensions of BSA-capped GNC, was investigated employing an indirect commercial enzymatic colorimetric method measuring $[H_2O_2]$. Since, within the sensitivity of the method, no traces of formed H_2O_2 were observed for both particle suspensions, it was assumed that $[O_2^-] \ll 1 \times 10^{-5}$ M.

3.3. Toxicity

3.3.1. Cytotoxicity and photodynamic activity of BSA-capped GNC in suspension

For the cytotoxicity determinations two human cell lines were used. On one hand, HaCaT was used as model of skin cell line, which are immortalized keratinocytes, non tumoral. On the other hand, HeLa, a classic tumor cell line used for testing potential PDT effectors, was used to contrast the effects with HaCaT.

The results of the biochemical assays performed in darkness and after irradiation in HeLa and HaCaT cells are presented in Figs. 9 and 10. The cell viability was measured by MTT and NR assays after 24 h of treatment. The MTT assay is based on the measurement of the mitochondrial succinate dehydrogenase activity of cells [46], while NR uptake and retention into the cell depends on the ability of the cell to maintain pH gradients through ATP production [47], staining primarily the lysosomes. By combining these methods, we aimed to obtain a better understanding of the interaction between the formulation and cells.

In Fig. 9A), it can be seen that for MTT testing, non-irradiated HeLa cells did not present significative differences with respect to their control, although at the maximum concentration tested (1000 μM of Au in BSA-capped GNC) viability apparently starts to diminish. On the other hand, for irradiated HeLa cells, only the minimum concentration (2.5 μM of Au) was not different from the control experiment. From 25 μM on, two effects were observed: firstly, the viability was clearly lower with respect to the control, and secondly, the difference in viability between the irradiated and non-irradiated cells gradually increased.

MTT assay on HaCaT cells is shown in Fig. 9B). For all concentration tested, both in the presence or absence of irradiation, a significative lowering of toxicity was determined. Remarkably, for low concentrations of BSA-capped GNC, toxicity was significantly higher for irradiated cells than for non-irradiated (see the internal comparison for 0.05 and 0.5 μM of Au). At higher concentrations, there are no significative differences in toxicity for irradiated cells respect to non-irradiated; thus, the lowering of viability between 50 and 500 μM of Au could be due only to intrinsic toxicity. This apparent recovery of

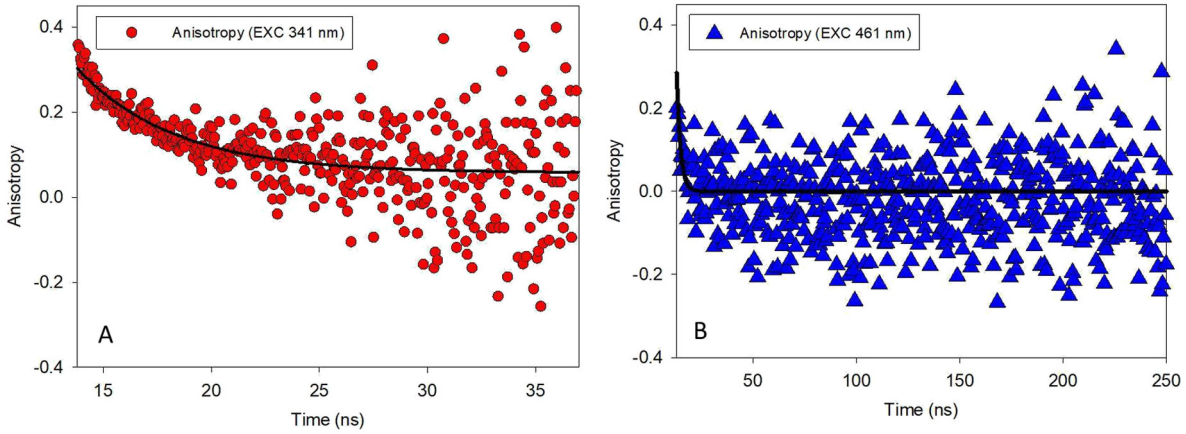

Fig. 5. Time-domain anisotropy decay of BSA-capped GNC. Graph (A) exciting with 341 nm and Graph (B) exciting with 461 nm. The emission was detected at 640 in both cases.

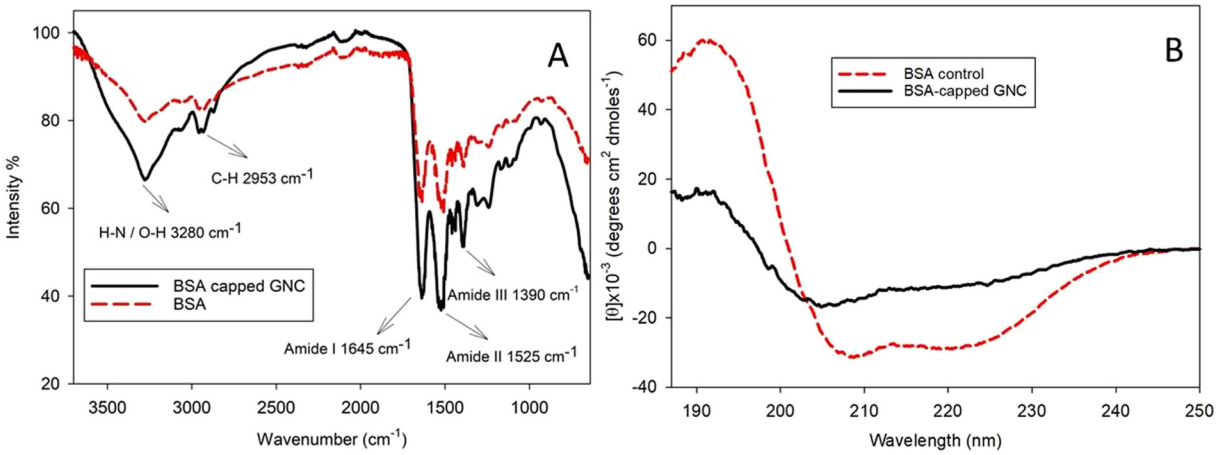

Fig. 6. Graph (A) FT-IR spectrum of BSA (red dotted line) and BSA-capped GNC (black line) obtained in KBr pellets as support. Graph (B) Far-DC spectra of BSA native (black line) and BSA-capped GNC (red dotted line) in PBS buffer 10 mM. (For interpretation of the references to colour in this figure legend, the reader is referred to the web version of this article.)

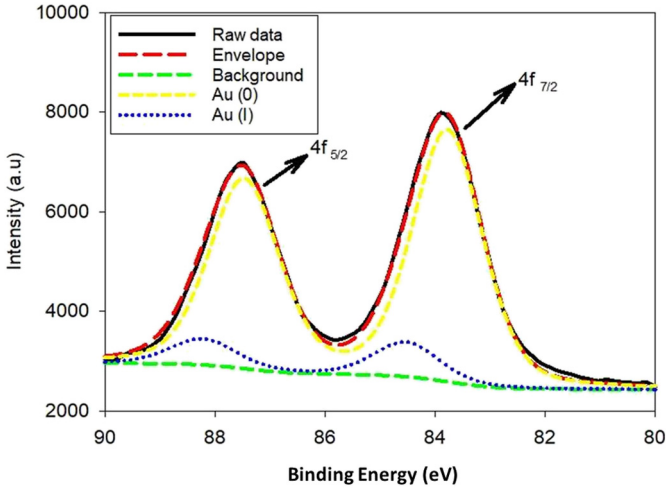

Fig. 7. Au 4f X-ray photoelectron spectra of as-prepared BSA-capped GNC.

viability of irradiated cells at higher concentrations could be due to the protective effect addressed to BSA and previously reported [48]. For NR assays, no toxic effects were seen for any of the tested conditions on both cell lines (Fig. 10), except for the maximum concentration in HaCaT cells (Fig. 10B).

In summary, these assays suggest that in some cases, singlet oxygen production caused certain toxic effects on both cell lines, but it was insufficient for induction of general toxicity, under the tested conditions. MTT could demonstrate the induction of alterations in the metabolism of both HeLa and HaCaT cells, although in different ranges of concentrations. The negative results of NR assays showed that pH gradients were not affected at the studied range. The differences observed between MTT and NR results could be addressed to the fact that MTT can be an early reporter of toxicity, while the drastic effects detected by NR could be evidenced only after longer incubations.

3.3.2. *Toxicity in zebrafish larvae*

Zebrafish larvae did not die after the experiments at the tested doses. The spontaneous movement was significantly diminished when incubated with BSA-capped GNC at a concentration of 60 μM, for all incubation times (Fig. 11). At the highest tested concentration—120 μM, no significant alterations in swimming respect to the control were observed, probably due to aggregation of the clusters. Another reason for the apparent recovery of the swimming activity at the highest concentration tested could be related to the protective effect addressed to BSA mentioned before in the cytotoxicity determinations.

3.4. *Skin penetration and cell capture by CLSM*

The assays with the SPM followed by tape stripping showed the access of BSA-capped GNC to the shallow SC (tapes 1–5), medium SC

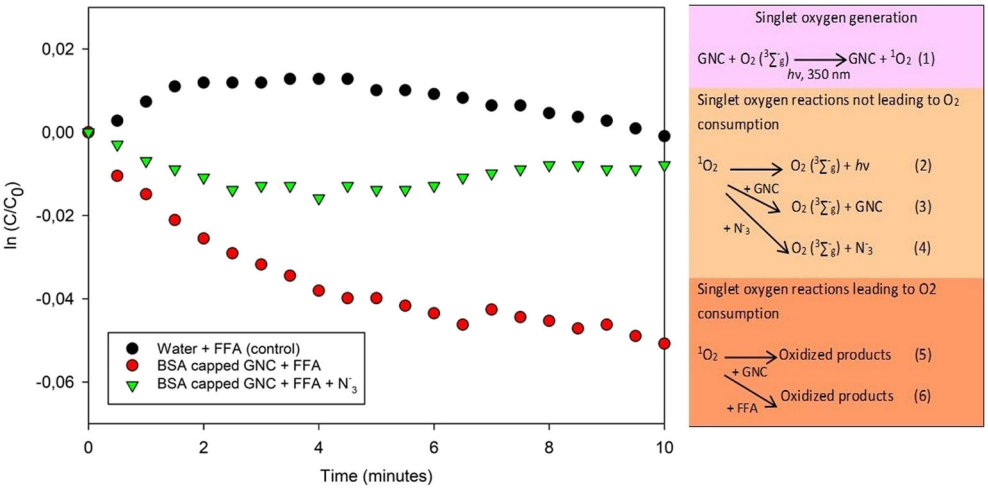

Fig. 8. Molecular oxygen consumption during irradiation at 350 nm of air-saturated aqueous suspensions of water + FFA (black circles), BSA-capped GNC with 10^{-3} M FFA (red circles) and BSA-capped GNC with 10^{-3} M FFA and 10^{-2} M azide (green triangles). The reactions in each experiment are also shown in the panel at the right. (For interpretation of the references to colour in this figure legend, the reader is referred to the web version of this article.)

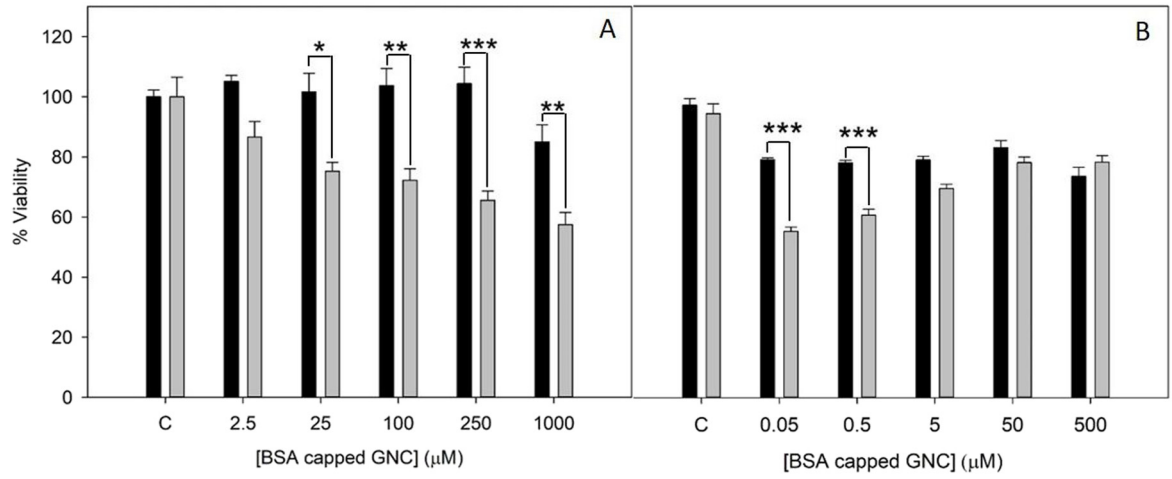

Fig. 9. MTT assay after 24 h of incubation with BSA-capped GNC on HeLa (A) and HaCaT (B). Dark and light gray bars correspond to non-irradiated and irradiated cells, respectively. Data are shown as mean ± SD (***$p < 0.0001$, **$p < 0.001$, *$p < 0.01$). Measurements were carried out in triplicate. Statistical differences between all treatments and their respective controls are not shown in the figure but describe in the text.

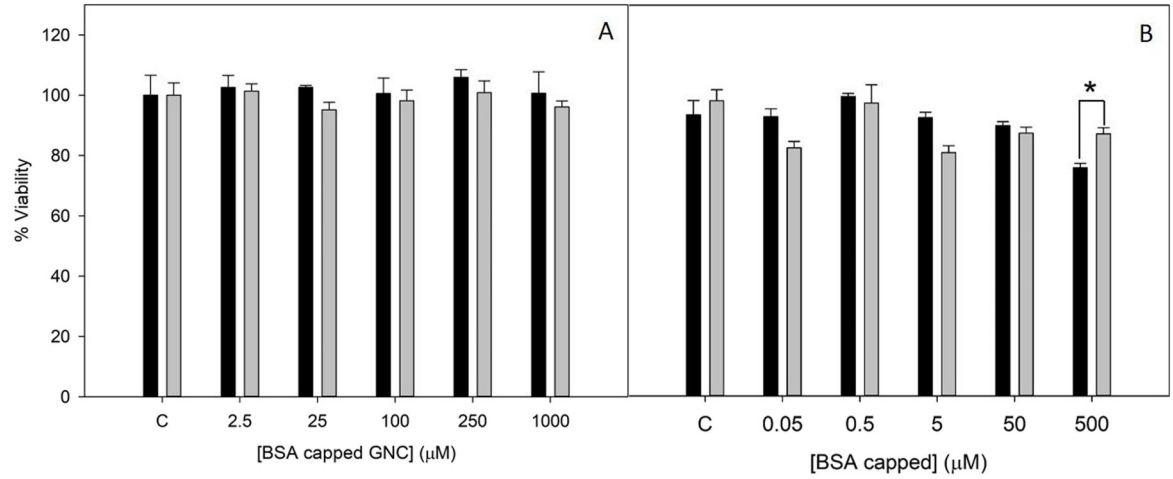

Fig. 10. NR assay after 24 h of incubation with BSA capped GNC on HeLa (A) and HaCaT (B). Dark and light gray bars correspond to non-irradiated and irradiated cells, respectively. Data are shown as mean ± SD (*$p < 0.01$). Measurements were carried out in triplicate. Statistical differences between all treatments and their respective controls are not shown in the figure but describe in the text.

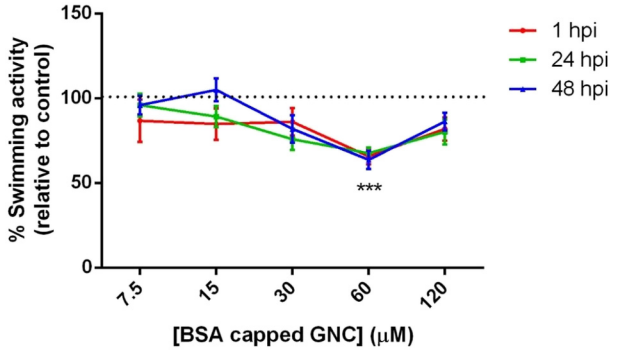

Fig. 11. Swimming activity of larvae as a function of BSA-capped GNC concentration, at 1, 24, and 48 h post-incubation (hpi). Values are relativized as a percentage of the swimming activity respect to the control and presented a mean ± SEM (***$p < 0.0001$), $n = 24$. Measurements were carried out in triplicate. The dotted line represents the activity of the control.

(tapes 6–10), deep SC (tapes 11–20), and viable epidermis + dermis, after 1 h of incubation (Fig. 12A).

CLSM images confirmed the penetration of the BSA-capped GNC into the explants (Fig. 12B). The transversal sections of the skin showed the fluorescence distributed along the SC region, also accumulating into the viable epidermis. CLSM analysis of incubated monolayers also registered fluorescence emission from the BSA-capped GNC in all HaCaT cells (Fig. 13). Remarkably, the internal fluorescence transfer revealed by photoluminescence experiments (Figs. 1 and 2) allowed the excitation of samples with a low wavelength laser (normally intended for DAPI excitation) and to collect a high emission with a wide peak separation, at 647 nm. This unique properties of these BSA-capped GNC could be useful for imaging when inserted in complex media as the skin tissue, with low chances to get false positives due to autofluorescence or to the emission of other particles involved, which is another indicator as the potential use of BSA-capped GNC in theragnostic approaches.

4. Conclusions

BSA-capped GNC, containing approximately one protein molecule for each Au_{25} cluster, can be excited in the UV region to render a fluorescent emission of red light. This could be due to an energy transfer from smaller GNC formed during this synthesis process and also possibly from the oxidized residues of BSA, which fluorescent emission after UV excitation overlays the excitation range of the Au_{25} clusters.

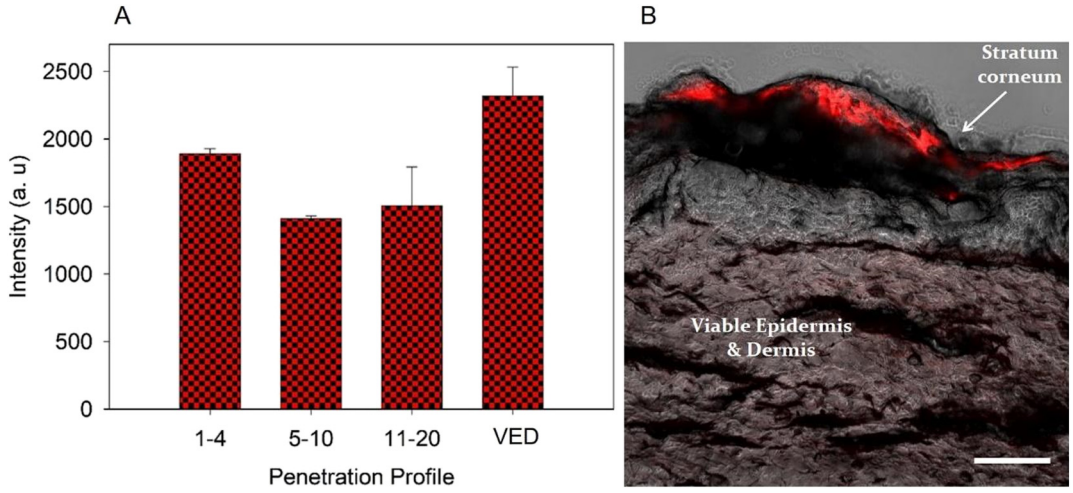

Fig. 12. (A) Penetration profile through human skin by tape stripping. The presence of BSA-capped GNC was determined in the upper stratum corneum (SC; tapes 1–4), middle SC (5–10), lower SC (11 − 20) and VED. Results are shown as mean ± SD (n = 5). (B) Confocal laser scanning microscopy (CSLM) images of cryosectioned skin after 1 h of incubation with BSA-capped GNC. Scale bar corresponds to 100 μm.

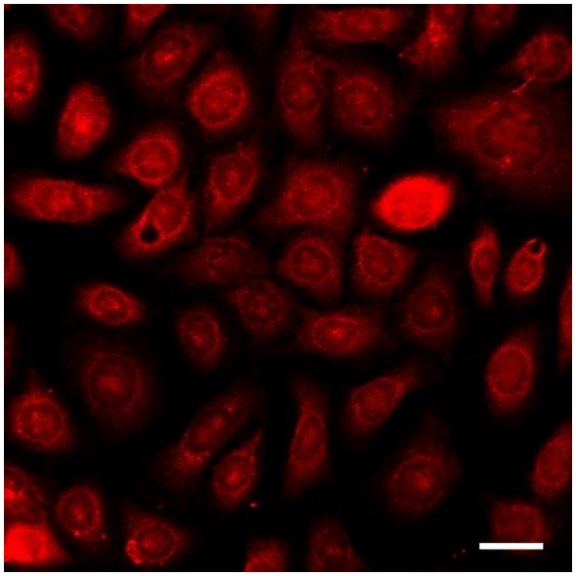

Fig. 13. CSLM image of HaCaT cells incubated with 100 μM of BSA-capped GNC. Picture confirms the cell uptake of the fluorescent nanoclusters. Scale bar corresponds to 20 μm.

On the other hand, BSA-capped GNC did generate singlet oxygen, in enough amount to lower the viability of cell cultures exposed to innocuous doses of 400 nm-wavelength irradiation. At the lowest concentrations in which those events took place, the viability in an *in vivo* model was not affected. BSA-capped GNC did penetrate the skin beyond the *stratum corneum* barrier.

In summary, for the first time we have demonstrated that BSA-capped GNC can behave as a bifunctional nanosystem, presenting at the same time potential as PDT effectors and as fluorescent biomarkers. This theragnostic potential could be useful in relation to diverse skin diseases. Further research could be focused on the coupling with molecules that allow their selective addressing and to enhance the reactive species generation by energy transfer.

CRediT authorship contribution statement

Cristian R. Lillo: Conceptualization, Methodology, Formal analysis, Investigation, Visualization, Validation, Writing - original draft. **Natalia Calienni:** Formal analysis, Investigation, Validation, Writing - review & editing. **Belen Rivas Aiello:** Formal analysis, Investigation. **M. Jimena Prieto:** Methodology, Investigation, Formal analysis. **Damián Rodriguez Sartori:** Investigation, Formal analysis. **Jimena Tuninetti:** Investigation, Formal analysis. **Pamela Toledo:** Investigation, Formal analysis. **Silvia del Valle Alonso:** Resources, Writing - review & editing. **Sergio Moya:** Resources, Writing - review & editing. **Mónica C. Gonzalez:** Conceptualization, Resources, Writing - review & editing. **Jorge Montanari:** Methodology, Conceptualization, Writing - original draft, Writing - review & editing, Resources. **Galo J.A.A. Soler-Illia:** Conceptualization, Supervision, Writing - review & editing, Funding acquisition, Resources, Project administration.

Declaration of competing interest

The authors declare that they have no known competing financial interests or personal relationships that could have appeared to influence the work reported in this paper.

Acknowledgments

This work was supported by ANPCyT (PICT 2015-3526, PICT 2014-3687), Argentina, and also from Universidad Nacional de Quilmes (PUNQ 990/19).

References

[1] N. Kaur, R.N. Aditya, A. Singh, T. Kuo, Biomedical applications for gold nanoclusters: recent developments and future perspectives, Nanoscale 13 (302) (2018) 1–12.
[2] J. Yang, F. Wang, H. Yuan, et al., Recent advances in ultra-small fluorescent Au nanoclusters toward oncological research, NanoS 11 (2019) 17967–17980.
[3] C. Fu, C. Ding, X. Sun, A. Fu, Curcumin nanocapsules stabilized by bovine serum albumin-capped gold nanoclusters (BSA-AuNCs) for drug delivery and theranosis, Mater. Sci. Eng. C. 87 (2018) 149–154.
[4] M. Zhu, C.M. Aikens, F.J. Hollander, G.C. Schatz, Correlating the crystal structure of a thiol-protected Au_{25} cluster and optical properties, J. Am. Chem. Soc. 130 (18) (2008) 5883–5885.
[5] J. Zheng, P.R. Nicovich, R.M. Dickson, Highly fluorescent noble-metal quantum dots, Annu. Rev. Phys. Chem. 58 (2007) 409–431.
[6] C. Kirchner, T. Liedl, S. Kudera, et al., Cytotoxicity of colloidal CdSe and CdSe/ZnS nanoparticles, Nano Lett. 5 (2) (2005) 331–338.
[7] Y. Pan, S. Neuss, A. Leifert, et al., Size-dependent cytotoxicity of gold nanoparticles, Small 3 (11) (2007) 1941–1949.
[8] Y. Zhang, C. Zhang, C. Xu, et al., Ultrasmall Au nanoclusters for biomedical and biosensing applications: a mini-review, Talanta 200 (2019) 432–442.
[9] L. Hu, S. Han, S. Parveen, Y. Yuan, L. Zhang, G. Xu, Biosensors and bioelectronics highly sensitive fluorescent detection of trypsin based on BSA-stabilized gold

nanoclusters, Biosens. Bioelectron. 32 (1) (2012) 297–299.
[10] X. Le Guével, B. Hötzer, G. Jung, M. Shneider, NIR-emitting fluorescent gold nanoclusters doped in silica nanoparticles, J. Mater. Chem. 21 (2011) 2974–2981.
[11] T. Zhou, Y. Huang, W. Li, et al., Facile synthesis of red-emitting lysozyme-stabilized Ag nanoclusters, Nanoscale 4 (2012) 5312–5315.
[12] X. Wang, Q. Wu, Z. Shan, Q. Huang, BSA-stabilized Au clusters as peroxidase mimetics for use in xanthine detection, Biosens. Bioelectron. 26 (2011) 3614–3619.
[13] G. Ma, A. Binder, M. Chi, C. Liu, R. Jin, D. Jiang, Stabilizing gold clusters by heterostructured transition-metal oxide-mesoporous silica supports for enhanced catalytic activities for CO oxidation, Chem. Commun. 48 (2012) 11413–11415.
[14] X. Liu, C. Li, J. Xu, et al., Surfactant-free synthesis and functionalization of highly fluorescent gold quantum dots, J. Phys. Chem. C 112 (29) (2008) 10778–10783.
[15] L. Shang, R.M. Dörlich, S. Brandholt, et al., Facile preparation of water-soluble fluorescent gold nanoclusters for cellular imaging applications, Nanoscale 3 (5) (2011) 2009–2014.
[16] X. Kang, H. Chong, M. Zhu, Au25(SR)18: the captain of the great nanocluster ship, Nanoscale 10 (23) (2018) 10758–10834.
[17] C.R. Lillo, M. Natalia Calienni, R.M. Gorojod, et al., Toward biomedical application of amino-functionalized silicon nanoparticles, Nanomedicine 13 (11) (2018) 1349–1370.
[18] N. Hodgkinson, C.A. Kruger, M. Mokwena, H. Abrahamse, Cervical cancer cells (HeLa) response to photodynamic therapy using a zinc phthalocyanine photosensitizer, J. Photochem. Photobiol. B Biol. 177 (2017) 32–38.
[19] J. Montanari, C. Maidana, M.I. Esteva, C. Salomon, M.J. Morilla, E.L. Romero, Sunlight triggered photodynamic ultradeformable liposomes against Leishmania braziliensis are also leishmanicidal in the dark, J. Control. Release 147 (3) (2010) 368–376.
[20] I.P. Hernández, J. Montanari, W. Valdivieso, M.J. Morilla, E.L. Romero, P. Escobar, In vitro phototoxicity of ultradeformable liposomes containing chloroaluminum phthalocyanine against New World Leishmania species, J. Photochem. Photobiol. B Biol. 117 (2012) 157–163.
[21] Vankayala R, Kuo C, Nuthalapati K, Chiang C. Nucleus-targeting gold nanoclusters for simultaneous in vivo fluorescence imaging, gene delivery, and NIR-light activated photodynamic therapy. , 5934–5945 (2015).
[22] H. Kawasaki, S. Kumar, G. Li, et al., Generation of singlet oxygen by photoexcited $Au_{25}(SR)_{18}$ clusters, Chem. Mater. 26 (2014) 2777–2788.
[23] P. Liu, W. Yang, L. Shi, et al., Concurrent photothermal therapy and photodynamic therapy for cutaneous squamous cell carcinoma by gold nanoclusters under a single NIR laser irradiation, J. Mater. Chem. B 7 (2019) 6924–6933.
[24] T. Das, P. Ghosh, M. Shanavas, A. Maity, S. Mondal, P. Purkayastha, Nanoscale protein-templated gold nanoclusters: size dependent inversion of fluorescence emission in the presence of molecular oxygen, Nanoscale. 4 (2012) 6018–6024.
[25] R. Gupta, B. Rai, Penetration of gold nanoparticles through human skin: unraveling its mechanisms at the molecular scale, J. Phys. Chem. B 120 (2016) 7133–7142.
[26] C.S. Martinez, D. Feas, M. Siri, D.E. Igartúa, V.A. Chiaramoni S del, M.J. Prieto, In vivo study of teratogenic and anticonvulsant effects of antiepileptics drugs in zebrafish embryo and larvae, Neurotoxicol. Teratol. 66 (2017) 17–24.
[27] M.N. Calienni, M. Cagel, J. Montanari, et al., Zebrafish (Danio rerio) model as an early stage screening tool to study the biodistribution and toxicity profile of doxorubicin-loaded mixed micelles, Toxicol. Appl. Pharmacol. 357 (2018) 106–114.
[28] A.M. Brouwer, Standards for photoluminescence quantum yield measurements in solution (IUPAC Technical Report), Pure Appl. Chem. 83 (12) (2011) 2213–2228.
[29] E. Panzarini, B. Tenuzzo, L. Dini, Photodynamic therapy-induced apoptosis of HeLa cells, Ann. N. Y. Acad. Sci. 1171 (2009) 617–626.
[30] U. Schaefer, H. Loth, An ex-vivo model for the study of drug penetration into human skin, Pharmacol. Res. 13 (Suppl., 366) (1996).
[31] M.N. Calienni, C.F. Temprana, M.J. Prieto, et al., Nano-formulation for topical treatment of precancerous lesions: skin penetration, in vitro, and in vivo toxicological evaluation, Drug Deliv Transl Res 8 (3) (2017) 496–514.
[32] J. Lademann, U. Jacobi, C. Surber, H. Weigmann, J.W. Fluhr, The tape stripping procedure — evaluation of some critical parameters, Eur. J. Pharm. Biopharm. 72 (2) (2009) 317–323.
[33] P. Bucci, M.J. Prieto, L. Milla, et al., Skin penetration and UV-damage prevention by nanoberries, J. Cosmet. Dermatol. 17 (5) (2017) 889–899.
[34] M.N. Calienni, C.R. Lillo, M.J. Prieto, R.M. Gorojod, Comparative toxicity of PEG and folate-derivated blue-emitting silicon nanoparticles: in vitro and in vivo studies, Nanomedicine (Lond) 14 (4) (2019) 375–385.
[35] J. Xie, Y. Zheng, J.Y. Ying, Protein-directed synthesis of highly fluorescent gold nanoclusters, J. Am. Chem. Soc. 131 (3) (2009) 888–889.
[36] K. Chaudhari, P.L. Xavier, T. Pradeep, Understanding the evolution of luminescent gold quantum clusters in protein templates, ACS Nano 5 (11) (2011) 8816–8827.
[37] X. Liu, T. Wang, T. Shu, et al., Combination of chemical etching of gold nanoclusters with aggregation-induced emission for preparation of new phosphors for development of UV-driven phosphor-converted white light-emitting diodes, J. Mater. Chem. C 4 (2016) 11482–11487.
[38] T. Shu, J. Wang, L. Su, X. Zhang, Chemical etching of bovine serum albumin-protected Au_{25} nanoclusters for label-free and separation-free ratiometric fluorescent detection of tris (2-carboxyethyl)phosphine, Anal. Chem. 88 (22) (2016) 11193–11198.
[39] L.K. Fraiji, D.M. Hayes, T.C. Werner, Static and dynamic fluorescence quenching experiments for the physical chemistry laboratory, J. Chem. Educ. (6) (1992) 424–428.
[40] S. Vogel, C. Thaler, P. Blank, S. Koushik, Time-resolved fluorescence anisotropy, FLIM Microscopy in Biology and Medicine, 2009, pp. 245–305.
[41] Y. Yue, H. Li, T. Liu, Y. Wu, Exploring the role of ligand-BSA in the response of BSA-protected gold-nanoclusters to silver(I) ions by FT-IR and circular dichroism spectra, Vib. Spectrosc. 74 (2014) 137–141.
[42] X. Cao, H. Li, Y. Yue, Y. Wu, Vibrational spectroscopy pH-induced conformational changes of BSA in fluorescent AuNCs @ BSA and its effects on NCs emission, Vib. Spectrosc. 65 (2013) 186–192.
[43] X. Wang, A. Ai, Z. Yu, et al., Dual-modal non-invasive imaging in vitro and in vivo monitoring degradation of PLGA scaffold based gold nanoclusters, Mater. Sci. Eng. C. 107 (2019) 110307.
[44] C.R. Lillo, J.J. Romero, M.L. Portolés, R.P. Diez, P. Caregnato, M.C. Gonzalez, Organic coating of 1–2-nm-size silicon nanoparticles: effect on particle properties, Nano Res. 8 (6) (2015) 2047–2062.
[45] L. Xiao, G. Luo, S. Howell, M. Sailor, Porous silicon nanoparticle photosensitizers for singlet oxygen and their phototoxicity against cancer cells, ACS Nano 5 (5) (2011) 3651–3659.
[46] R. Supino, MTT assays, in: S. O'Hare, C.K. Atterwill (Eds.), In Vitro Toxicity Testing Protocols. Methods in Molecular Biology, Humana Press, 1995, pp. 137–149.
[47] G. Repetto, A. del Peso, J.L. Zurita, Neutral red uptake assay for the estimation of cell viability/cytotoxicity, Nat. Protoc. 3 (7) (2008) 1125–1131.
[48] L. Dong, M. Li, S. Zhang, et al., Cytotoxicity of BSA-stabilized gold nanoclusters: in vitro and in vivo study, Small 11 (21) (2015) 2571–2581.